Coupling time-resolved PIV flow-fields and phase-invariant proper orthogonal decomposition for the description of the parameters space in a Diesel engine

Imran Cosadia[1], Jacques Borée[2], Patrick Dumont[3]

1: Department of Fluid Mechanics & Combustion, Renault s.a.s., Lardy, France, imran.cosadia@renault.com
2: Laboratoire d'Etudes Aérodynamiques, Ensma UMR Cnrs 6609, Poitiers, France, jacques.boree@lea.ensma.fr
3: Department of Fluid Mechanics & Combustion, Renault s.a.s., Lardy, France, patrick.dumont@renault.com

Abstract Particle image velocimetry (PIV) results obtained from one Diesel transparent engine with a cylindrical bowl-in piston are investigated in this paper. Beyond the standard statistical description of in-cylinder flows, time-resolved PIV (TRPIV) now allows to access the in - cycle evolution. To describe the large-scale motions and to reveal the flow dynamics, it is necessary to combine in an optimal way the statistically converged PIV datasets and the limited number of in-cycle TRPIV measurements. A new coupling approach between these TRPIV data and phase-invariant proper orthogonal decomposition (POD) is proposed in this aim. The POD modes resulting from the decomposition of the first dataset are used as an energetic basis for the projection of the time-resolved flow-fields during the whole compression stroke. This original method allows to solve cycle-to-cycle variations, to describe the parameters space for a relevant number of flow realisations and finally to examine the in-cycle evolution of the POD random coefficients.

1. Introduction

Air motion within Diesel cylinder critically affects the combustion quality and pollutant emissions (Heywood 1988, Payri et al. 1996). In Diesel applications, a specific mean flow, called "swirl" is often induced in the cylinder. The charge rotates around an axis parallel to the cylinder axis and is being compressed under the piston displacement. The idea behind the swirl induction is to encapsulate some of the momentum of the inlet valve air jets in a large rotating coherent motion, which is less dissipative than turbulence, and hence will retain energy longer. To comply with severe pollution reduction requirements, the large-scale rotating air motion is also introduced into the combustion chamber so that the fuel spray is correctly mixed during the injection process. The angular momentum of this induced air motion must be large enough to ensure good transport properties but not so large that spray plumes overlap. These features have to be the same from one cycle to the other. Unfortunately, cyclic variations occur most of the time in the combustion chamber (Enotiadis 1990). There exist therefore differences between consecutive or non - consecutive cycles, which are harmful to the combustion efficiency. Thus, engine design must take into consideration the large-scale fields' repeatability, since this will obviously affect efficiency, fuel consumption and emissions.

Even if the importance of in-cylinder flow was recognized quite early, one had to wait for the development of optical diagnostic techniques and especially for laser Doppler velocimetry (LDV) to obtain detailed measurements in combustion chambers (Arcoumanis and Whitelaw 1987; Hill and Zhang 1994; Payri et al. 1996). Local measurements of one or two components of the velocity fields are most often obtained in chosen points and provide useful information about the structure of the flow and the state of turbulence. It is however very difficult to understand the instantaneous spatial structure of the flow from these data. Visualization tools and optical methods were then adapted to allow a better understanding of the physical process implied in those complex flows.

Particle image velocimetry (PIV) is such a complementary technique. PIV of in-cylinder flow was pioneered by (Reuss et al. 1989). Spatial filtering was used in these early works to distinguish between large-scale and small-scale features. Applied to in-cylinder flow, PIV provides a clearer

description of the structure of the flow field in transparent research engines (Baby 1997; Borée et al. 2003). It is becoming now an efficient investigation tool in the industry. Most of the time, PIV has been applied on gasoline engine. Due to thermodynamical and geometrical constraints (confining effect), it was difficult to apply such techniques to Diesel engines which have a high compression ratio. Many efforts have been made to overcome those issues. The research engine from which we got the results presented here has been built by RENAULT s.a.s. in order to improve the understanding of the flow structure and the cyclic variations of the swirling flow.
In the context of analyzing the statistical properties of the swirl, proper orthogonal decomposition (POD) is often applied to PIV datasets. The POD was proposed in (Lumley 1967) to extract coherent structures from turbulent flows. This method is objective since the decomposition functions are not of pre-determined form, but constructed through an optimization process. It is optimal as far as the kinetic energy contained in the successive modes is concerned. This statistical tool is now widely applied for analyzing experimental data obtained with PIV or rakes of hot wires. It can also be useful for extracting relevant information from the large amount of data obtained with direct numerical simulation (DNS) or large eddy simulation (LES). When most kinetic energy in the flow domain analyzed by the POD is embedded in a large-scale rotating structure, a common result is that low-order modes are associated with temporal and cyclic variation of the structure. In a well-defined rotating flow, (Graftieaux et al. 2001) have shown that three modes are sufficient to characterize the vortex wandering. Note that POD was also used in order to provide a description of the flow dynamics (Berkooz et al. 1993) and that a phase invariant POD specially designed to offer a rigorous description of the parameter spaces in engine flows was recently proposed by (Fogleman et al. 2004). This tool will be used in the present work.
Moreover, beyond the standard statistical description of in-cylinder flows, time-resolved PIV (TRPIV) now allows to access the in-cycle evolution. TRPIV was successfully applied to gasoline engines. Temporal studies of the “tumble” flow have been performed (Druault et al. 2005) and “swirl” has also been investigated in a gasoline designed experiment (Towers et al. 2004). Unfortunately, because of measurements quality reasons and data storage limitations, TRPIV can only be obtained for a limited number of consecutive cycles. To precisely describe the dynamics of the compressed flow, it is therefore necessary to combine in an optimal way the statistically converged PIV data sets and the limited number of temporally solved TRPIV sets. In this aim, such a coupling approach between TRPIV measurements and phase invariant POD will be proposed.
Two different datasets were thus used for discussions. The first one is the statistically converged dataset we got from « standard » (2D2C PIV, low time resolution) PIV measurements, at a fixed plane, several fixed crank angle degrees (CAD), for consecutive engine cycles. This set was used in the computation of the phase-invariant POD modes. The second database contains the TRPIV measurements. The POD modes resulting from the decomposition of the first dataset are used as a projection basis for the TRPIV fields. These projections on the POD modes are then analyzed in the following to access the cyclic variability of the compressed flow. Moreover, we insist on the ability of the POD to examine some special behaviours of the compressed flow, seen as a dynamical system, in which the state corresponds to specific flow configurations.

2. Experimental set-up and measurements

Experimental set-up is a motored four valve single-cylinder engine with plate roof combustion chamber, which allows different compression ratios (from 12 to 21). The engine rotation speed has been fixed at 1200 rpm during all the experiments. The geometry tested, except for the piston shape, was a direct replica of a Diesel engine and operated at a compression ratio of 20:1.
The engine was constructed with a full stroke quartz cylinder enabling optical access. Horizontal measurement plane is examined by projecting the laser sheet through the quartz cylinder and imaging through the transparent piston via a mirror.

Bore b = $2R_c$	80mm	Bowl depth	15 mm
Stroke S	93 mm	Squish height	0,7 mm
Engine speed	1200 rpm	Maximum temperature at TDC	550°C
Bowl diameter $D_b = 2R_b$	38 mm	Maximum pressure at TDC	40 bars
Cylinder head	4-valve	Compression ratio	20

Table 1. Engine dimensions and characteristics.

PIV measurements through transparent piston with a real shape ("omega shape") are critical since optical distortions are very strong and cannot be rectified easily; the bowl is then cylindrical. Except for this piston shape, the single-cylinder engine has got the same features as a real engine. Since Diesel thermodynamic conditions are higher than spark ignition engine, developing new technologies concerning piston management appeared as a necessity. Piston rings with no lubrication permit to keep a right pressure inside cylinder without scratching glasses. Ring material must be heatproof since the in-cylinder temperature is up to 550°C. Its low coefficient of thermal expansion avoids engine jamming and ensures a low blow-by. Instead of a mechanical fixation for the transparent piston, a sticking-based technology developed by Renault s.a.s. was used, which allows a large visualization area. It also allows visualisation in bowl from all sides. The minimum area visualisation diameter is 71 mm. This diameter depends on the distance between horizontal measurement section and piston crown. Depending on the relative locations of piston and measurements planes, this diameter is varying from 71 mm to 80 mm (engine bore). Engine features have been summarized in table 1. However, note that the whole description of the test bench is beyond the scope of this paper. Measurements in the horizontal measurement plane (z = -7,5 mm) are discussed here. This plane located under the roof of the cylinder head is the median plane of the bowl at TDC (see Cosadia et al. 2006 for more details).

The visualization system used for the statistically converged dataset *(i)* differed from the one used in the time-resolved measurements *(ii)*.

(i) Statistically converged dataset : the PIV system used to obtain the first dataset consists in a double pulsed Nd:Yag laser and a Kodak CCD camera for image recording. The camera was operating with a spatial resolution of 1008 x 1018 pixels^2. The laser sheet has been adjusted to 1 mm. Synchronization with engine angular information and operation frequencies allowed having one measurement, i.e. one instantaneous velocity field, at every engine cycle. This is particularly useful to point out cyclic variations of the flow. The number of engine cycles per engine phase, i.e. the number of instantaneous fields is N=300. The number of cycles acquired is K=7, implying a total number of 2100 instantaneous velocity fields. From all the statistical measurements, the velocity vectors computation conditions were fixed for all the CAD acquired. Adaptive inter-correlation has been processed on 32 x 32 pixels^2-size final interrogation spots, with 50 % overlap, which gives a 62 x 62 vectors^2 grid. True size (without overlap) of the interrogation windows is $\Delta \approx 2.5mm$. Particle images treatment consists in using subpixel cell shifting and deformation, allowing bias and random error reduction (Lecordier 1997). A widely accepted estimation of the absolute displacement error using these algorithms is 0.05 pixels.

(ii) Time-resolved dataset : the high speed PIV system consists in a dual head Nd:Ylf laser, whom light sheet was also adjusted to 1 mm. The laser operates at 1 kHz. A 512x512 pixels^2 Nanosense ® (Dantec) CMOS camera was used. The decreasing of the sensor size (and then the spatial resolution) allows having a better time resolution. The laser energy was adjusted to 5 mJ to achieve good measurement quality from BDC to TDC. The inter-frame was adjusted to catch velocity gradients during both intake and compression strokes. Data were obtained during 12 consecutive

cycles every 4.8 CAD (~ 0.5 CAD of incertitude). In this context, we have 12 entire compression strokes, each of them consisting in 31 velocity fields; thus a total number of 372 fields since we focus only on the compression strokes. We also performed adaptive correlation from the second dataset. A matrix of 61x61 vectors is obtained, with a spatial resolution of 1.24 mm. True size of the interrogation windows is $\Delta \approx 4.96mm$.

In both cases, Dantec correlator ® was used. Vectors maps from *(i)* and *(ii)* were then submitted to specific treatments to reject spurious vectors. Standard validation criteria based on signal to noise ratio (minimal value of 1.21), velocity magnitude and comparison with the local median value (Westerweel 1993) on a 7x7 neighbourhood have been achieved as post-processing steps. The number of spurious vectors was always low (less than 1% of the whole vectors field). False vectors were replaced in both cases by the local median value, since it has visually proved to conserve the flow spatial coherence. No further filtering has been applied to the velocity fields in order to keep the whole measurement information. Note that optical deformations in our case are linked to the optical access. Indeed, the measurement plane is recorded through a cylindrical piston, which is a simplified shape compared to those commonly used in real engine piston configuration but entails even though optical deformations. Spherical aberration, field aberration and distortion have been estimated to give the particle position error. The effects of these optical aberrations were weak compared to the particle size. They were consequently not corrected, since they do not significantly affect the results. In the following, vectors will be denoted in bold. The symbol $\langle\ \rangle$ indicates an averaging operator. The symbol $\langle\ \rangle_\theta$ indicates phase-averaging operator. The reference frame was set so **x** leads the axis between the two intake ports. The origin $(x,y)=(0,0)$ is chosen in the middle of the cylinder. We denote $\mathbf{U}_n(\mathbf{x},\theta_m)$ the instantaneous velocity field from *(i)*, where $\mathbf{U}_n$ is the instantaneous velocity vector at the engine cycle *n*, with $n \in [1;300]$, θ_m the engine phase, with $m \in [1;7]$. Actually, from BDC to 220 CAD, the inlet valves are not completely closed, so that the total amount of energy embedded within the cylinder is still varying. We therefore consider the compression stroke only to occur between 220 and 360 CAD. The engine phases studied correspond in CAD to $\theta_1 = 220°$; $\theta_2 = 270°$; $\theta_3 = 300°$; $\theta_4 = 320°$; $\theta_5 = 335°$; $\theta_6 = 350°$ and $\theta_7 = 360°$ (TDC). We denote $\mathbf{U}^r{}_n(\mathbf{x},\theta)$ the instantaneous velocity vector from *(ii)*, where $n \in [1;12]$ is the engine cycle and θ takes 31 values during a compression stroke (between 216 and 360 CAD).

Applying PIV in a Diesel engine entails strong constraints on the seeding material. Solid particles were used to avoid burning the flow tracers. However, finding a solid material that could be introduced in the cylinder without damaging the quartz window and the piston rings was time consuming. The time response of the flow tracers used here in air at standard conditions (Atmospheric pressure, temperature equal to 20°C) is $\tau_p = \rho_p {d_p}^2 / 18\mu_a \approx 3.5 \times 10^{-4} s$, where ρ_p is the density of the beads, d_p their diameter. μ_a is the air viscosity. Note that μ_a is increasing during the compression stroke (the viscosity of the air globally evolves like the square root of the temperature inside the chamber, according to Sutherland's law). Consequently, the time response of the particles is decreasing between the bottom and the top dead center.

Four time scales have been compared to τ_p in order to evaluate the seeding quality for this engine flow : the engine time scale τ_e, the mean swirl turn-over time scale τ_S, the turbulent turn-over time scale τ_t and the turn-over time scale of small eddies of the size Δ of the PIV interrogation window τ_Δ. More details about this procedure can be found in (Cosadia et al. 2006). For each comparison, the particles used were proved to correctly track the large scale features of the flow.

Nevertheless, the spatial filtering induced by PIV and the temporal filtering due to the particles definitely prevent an accurate resolution of the turbulence spectrum in these measurements. This is not a real problem for this study because only large scale variability of the flow will be examined in

the following. Note that in the case of time-resolved measurements, seeding is one major task to overcome. Contrary to ensemble data where one snapshot is obtained at each CAD, in-cycle flow resolution prevents from optimizing seeding density in respect to the engine phase.

3. Phase-invariant proper orthogonal decomposition

To allow a complete description of the large-scale motions during the compression stroke by POD, it is necessary to obtain a common basis for all the compression phases. By a phase–dependant POD approach, one is able to get an optimal basis only for the engine phase at which the statistical sample is considered. Using a phase-invariant POD will eliminate the phase dependence of the modes. This method was introduced by (Fogleman et al. 2004) on a tumbling flow in a model engine. The statistical fields from the compression stroke must be put in common to build the correlation tensor **R**. This operation must be done carefully. Velocity fields must be fixed on a same adimensioned grid to correctly prepare the Dyadic product. For the four first phases, the flow fits the quasi–entire bulk of the cylinder (fig. 1).

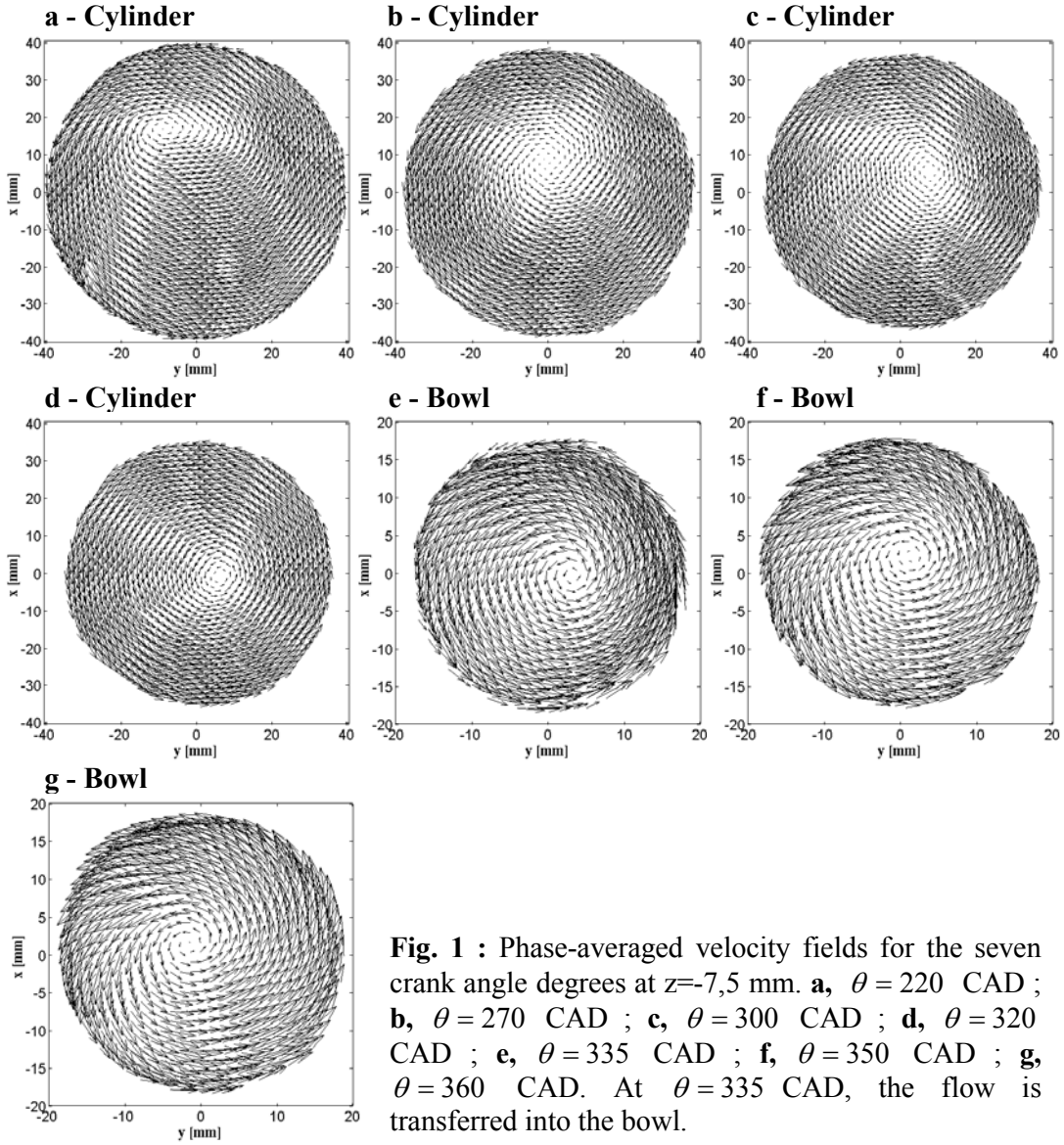

Fig. 1 : Phase-averaged velocity fields for the seven crank angle degrees at z=-7,5 mm. **a,** $\theta = 220$ CAD ; **b,** $\theta = 270$ CAD ; **c,** $\theta = 300$ CAD ; **d,** $\theta = 320$ CAD ; **e,** $\theta = 335$ CAD ; **f,** $\theta = 350$ CAD ; **g,** $\theta = 360$ CAD. At $\theta = 335$ CAD, the flow is transferred into the bowl.

The visualisation area is varying depending on the position of the piston. To overcome this difficulty, the velocity fields have a common mask and are projected on a unique meshgrid. The fields that fit the bowl (3) are stretched on the grid and a bidimensional spline cubic interpolation is performed to complete the vector fields. This interpolation method does not significantly affect the amount of energy contained within the bowl. Indeed, the small variation of energy that could result from that interpolation does not influence the main POD modes, which are suitable for a large-scale flow description. Moreover, we note that every engine phase is holding a different amount of kinetic energy (fig. 2a). Energy statistics are shown on figures 2b, 2c and 2d.

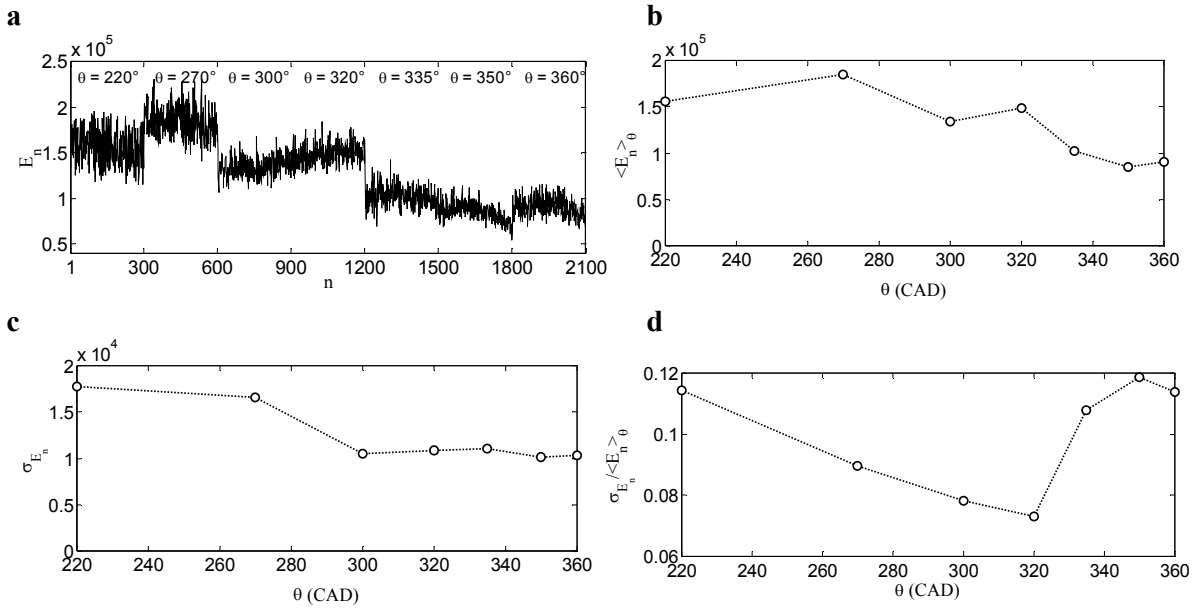

Fig. 2a-d. Energy statistics : **a,** $E_n(\theta)$; **b,** $\langle E_n \rangle_\theta$; **c,** σ_{E_n} ; **d,** Intensity $I(\theta) = \sigma_{E_n} / \langle E_n \rangle_\theta$

To eliminate this phase-to-phase energetic dispersion and to equally weight the phases of the flow, a specific normalization of each instantaneous velocity field *n* by the square root of its own kinetic energy E_n has been performed. The result is a normalized velocity field $\mathbf{u}_n(\mathbf{x}, \theta_m) = \mathbf{U}_n(\mathbf{x}, \theta_m) / \sqrt{E_n}$ corresponding to a new individual event having a normalised kinetic energy (Fogleman et al. 2004).POD modes are computed in the frame of the method of snapshots introduced by (Sirovich 1987). The two-point correlation tensor is approximated by :

$$\mathbf{R}(\mathbf{x},\mathbf{x}') = \langle \mathbf{u_n}(\mathbf{x}) \mathbf{u_n}(\mathbf{x}') \rangle = \frac{1}{M} \sum_{n=1}^{M} \mathbf{u_n}(\mathbf{x}) \mathbf{u_n}(\mathbf{x}') \qquad (1)$$

M is the total number of independent events in the PIV statistical dataset $(M = N \times K)$. Vector multiplication denotes a Dyadic product. The fields are all real, and the matrices symmetric, so that the eigenvectors and eigenvalues are real. M eigenfunctions $\mathbf{\Phi}^{(k)}(x,y)$ and positive eigenvalues $\Lambda^{(k)}$ ($k=1,\ldots M$) are obtained with : $\mathbf{\Phi}^{(k)}(x,y) = \sum_{n=1}^{M} c_n^{(k)} \mathbf{u_n}(x,y)$. The constants $c_n^{(k)}$ are eigenvectors of the matrix $C = \lfloor (\mathbf{u_n}, \mathbf{u_p}) / M \rfloor$ and $\Lambda^{(k)}$ correspond to the associated eigenvalues. Here, $(\mathbf{u_n}, \mathbf{u_p})$ denotes the inner product $(\mathbf{u_n}, \mathbf{u_p}) = \sum_{(x,y) \in S} \mathbf{u_n}(x,y) \mathbf{u_p}(x,y)$. Having solved the POD problem, each instantaneous flow field component belonging to the compression stroke can be

projected onto the POD basis to obtain:

$$\mathbf{u_n}(x,y) = \sum_{k=1}^{M} \alpha_n{}^{(k)} \mathbf{\Phi}^{(k)}(x,y) \qquad (2)$$

$\mathbf{\Phi}^{(k)}(x,y)$ *[k=1,M]* are the POD modes associated to the eigenvalues $\Lambda^{(k)}$. The eigenvalues are real and $\Lambda^{(k)} > \Lambda^{(k+1)}$. The modes form an orthonormal basis. Thus, we have: $\left(\mathbf{\Phi}^{(k)}, \mathbf{\Phi}^{(l)}\right) = \delta_{kl}$. $\alpha_n{}^{(k)} = \left(\mathbf{u_n}{}^{(k)}, \mathbf{\Phi}^{(k)}\right)$ are the random reconstruction coefficients. These coefficients are uncorrelated with $\left\langle \alpha_n{}^{(k)} \cdot \alpha_n{}^{(l)} \right\rangle = \Lambda^{(k)} \delta_{kl}$. This general statistical theory is well adapted to problems in turbulence study as it provides a diagonal decomposition of the correlation tensor and an optimal decomposition of the kinetic energy *[e=1]* integrated over the flow domain analyzed with POD :

$$e = \left\langle \left(\mathbf{u_n}, \mathbf{u_n}\right) \right\rangle = \sum_{k=1}^{M} \Lambda^{(k)} = 1 \qquad (3)$$

From the POD decomposition, some authors (see e.g. Bonnet et al. 2002 and references therein) propose to define a truncated velocity field $\mathbf{u_n}{}^{\leq m}(x,y)$ defined as a projection onto the *"m ≤ M"* first POD modes: $\mathbf{u_n}{}^{\leq m}(x,y) = \sum_{k=1}^{m} \alpha_n{}^{(k)} \mathbf{\Phi}^{(k)}(x,y)$. It is important to recall that the eigenvalues, in the frame of a normalised phase-invariant approach, represent the contribution of the mode to the structure of the flow, for all cycles and all phases of the compression stroke. These are therefore "global" quantities. The values of $\Lambda^{(k)}$ are listed in table 2 for k=1,...10. We have $\Lambda^{(1)} \approx 25\Lambda^{(2)}$ and $\Lambda^{(2)} \approx \Lambda^{(3)}$. The three first normalized phase-invariant eigenmodes have been presented in figure 3. The first eigenmode, which is the most energetic structure, represents 84 % of *e=1* and has the typical structure of a mean swirling flow. We recall that the term "mean" corresponds here to an averaging operation on all the fields belonging to the statistical dataset, i.e. a "mean compression" field (fig. 3a). The two following modes represent about 6% of the total kinetic energy. From these values, one can infer that the three first modes, which represent about 92% of *e*, might be sufficient to build a low-order model of the compressed swirling motion.

mode n°	1	2	3	4	5	6	7	8	9	10
$\Lambda^{(k)}$	0.872	0.033	0.019	0.007	0.004	0.003	0.003	0.002	0.002	0.002
$\sum_1^k \Lambda^{(k)}$	0.872	0.906	0.925	0.933	0.937	0.941	0.944	0.947	0.949	0.951

Table 2. POD spectrum and its convergence

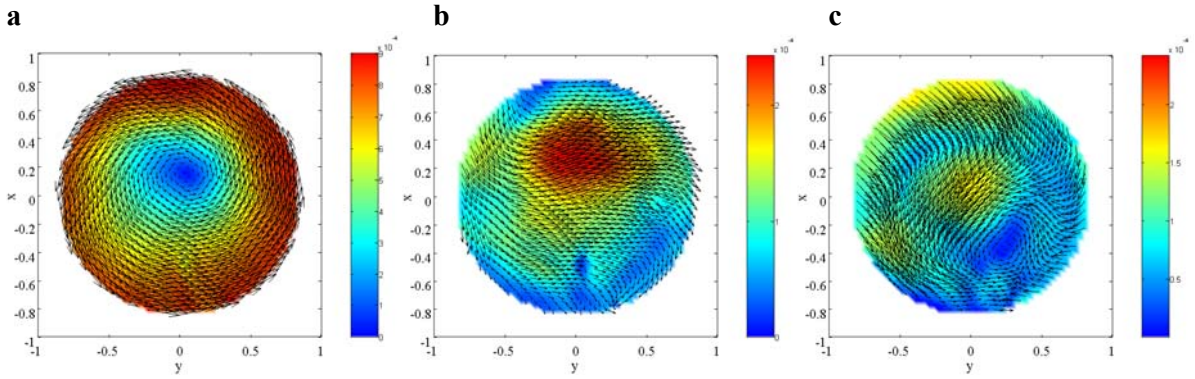

Fig. 3a-c. Normalized phase-invariant POD modes $\sqrt{\Lambda^{(k)}} \cdot \mathbf{\Phi}^{(k)}(x,y)$. **a**, k=1; **b**, k=2; **c**, k=3.

In the central region of the flow, the second and third normalized modes exhibit a high magnitude, which means that they contribute to a large-scale motion. The contribution of these phase-invariant modes can be quantified using statistically probable flow-fields (Patte-Rouland et al. 2001). Such procedure shows that mode 2 and mode 3 are linked with the displacement of the swirling motion inside the chamber. The second mode is characteristic of a displacement in a fixed direction and so is the third mode. Therefore, the coefficients associated with these two modes, $\alpha_n^{(2)}$ and $\alpha_n^{(3)}$, can be used to quantify the magnitude of the displacement in these last two privileged directions. The "classical" approach consists then in analyzing the evolution of the coefficients within the cycle, which could give a rough sketch of the compressed flow dynamics. But even though a phase-invariant approach is beneficial from a convergence point of view, it does not allow the investigation of the dynamics of individual cycles, since the snapshots are statistical and never time-resolved.

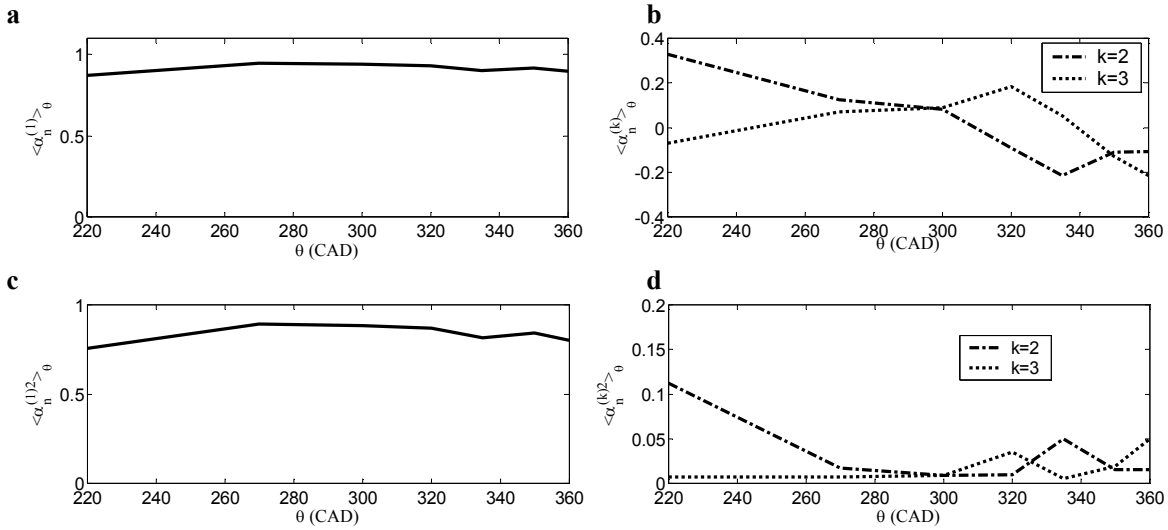

Fig. 4a-d. Evolution of $\left\langle \alpha_n^{(k)}(\theta_m) \right\rangle$ and $\left\langle \alpha_n^{(k)}(\theta_m)^2 \right\rangle$ for the first three modes.

Figures 4c-d show the evolution of $\left\langle \alpha_n^{(k)}(\theta_m)^2 \right\rangle_\theta$ for k=1, 2 and 3. Since $\alpha_n^{(1)}(\theta_m) > 0$, curves from figures 4a and 4c have the same evolution. Between $\theta = 270°$ and $\theta = 300°$, a maximum level of $\left\langle \alpha_n^{(1)^2} \right\rangle_\theta$ is observed, meaning that the structure of the flow is very close to the first POD mode. The rotation of the flow then would strongly dominate the in-cylinder flow evolution. The values of $\left\langle \alpha_n^{(k)^2} \right\rangle$ for k=2 and 3 reveal to be significant at the end of the stroke, from $\theta = 320°$ to TDC. A local peak of $\left\langle \alpha_n^{(2)^2} \right\rangle_\theta$ is observed at $\theta = 335°$, whereas the maximum value of the coefficient is found at the very beginning of the compression stroke. $\left\langle \alpha_n^{(3)^2} \right\rangle_\theta$ is reduced during the transfer, but reaches a maximum at TDC.

4. Coupling methodology and cyclic variations

Having "only" TRPIV data along 12 consecutive cycles, it would be impossible to compute a POD basis from these fields. Indeed, the convergence of the modes would be very poor. Performing a

phase-invariant POD approach allows to have statistically converged modes. A total of 2100 snapshots from the PIV data have been used. All these snapshots are independent as the data from each phase are from a different ensemble of cycles. The approach we propose here consists in using this statistically converged dataset combined with a set of temporal measurements obtained within the engine cycles. The modes obtained by phase-invariant POD are a basis for the whole compression stroke and will be used as a decomposition basis for the velocity fields resulting from TRPIV measurements. This technique allows building a decomposition of the spatio-temporal complexity of the flow field into elementary modes. We are then able to catch the temporal dynamics of the flow-field by following the evolution of the decomposition coefficients, obtained as the projection of the time-resolved fields on the phase–invariant eigenmodes :

$$a_n^{(k)}(\theta_m) = \left(\mathbf{u}'_n(\mathbf{x},\theta_m), \mathbf{\Phi}^{(k)}(\mathbf{x})\right) \quad [k=1,M; n=1,N; m=1,K] \qquad (4)$$

Where $\mathbf{u}'_n(\mathbf{x},\theta_m)$ is the time-resolved flow field at the engine phase $\theta=\theta_m$, in the cycle *n*, normalized by the square root of its kinetic energy and $\mathbf{\Phi}^{(k)}(\mathbf{x})$ is the phase-invariant mode number *k*. Since the phase–invariant modes are obtained only on seven characteristic phases of the compressed flow, the projections $a_n^{(k)}(\theta_m)$ will be examined only at these CAD. However, our temporal resolution allows to follows the flow at a faster rate than the crank angle sampling used in the statistical database. Therefore, it could be quite interesting to take into account the intermediate CAD. This procedure would be introduced as an interpolation method to recover more accurately the swirling flow dynamics. It would allow having a better understanding of the dynamics, especially of what is happening when the piston reaches TDC, at the very top of the piston crown. This approach is straightforward when POD is used (Druault et al 2005) but will not be considered in the following.

The figures 5a, b, c show the evolution of $\left[a_n^{(k)}(\theta)\right]^2$ for k=1, 2 and 3 and $\theta \in [220°,360°]$. The mean and RMS values of $\left[a_n^{(k)}(\theta)\right]^2$ are also shown. The dispersion of $a_n^{(1)}$ and $a_n^{(2)}$ is quite large at $\theta = 220°$, which means that the structure of the flow near BDC is complex. The RMS values are very small at $\theta = 300°$ and $a_n^{(1)}$ clearly dominates. A strong dispersion of the three projection coefficients is then detected during the transfer in the bowl (peak of $\left[a_n^{(3)}(\theta)\right]^2$ at $\theta = 320°$ just before the transfer) and the RMS is high at TDC. The structure of the swirling motion at TDC therefore changes considerably from one cycle to another.

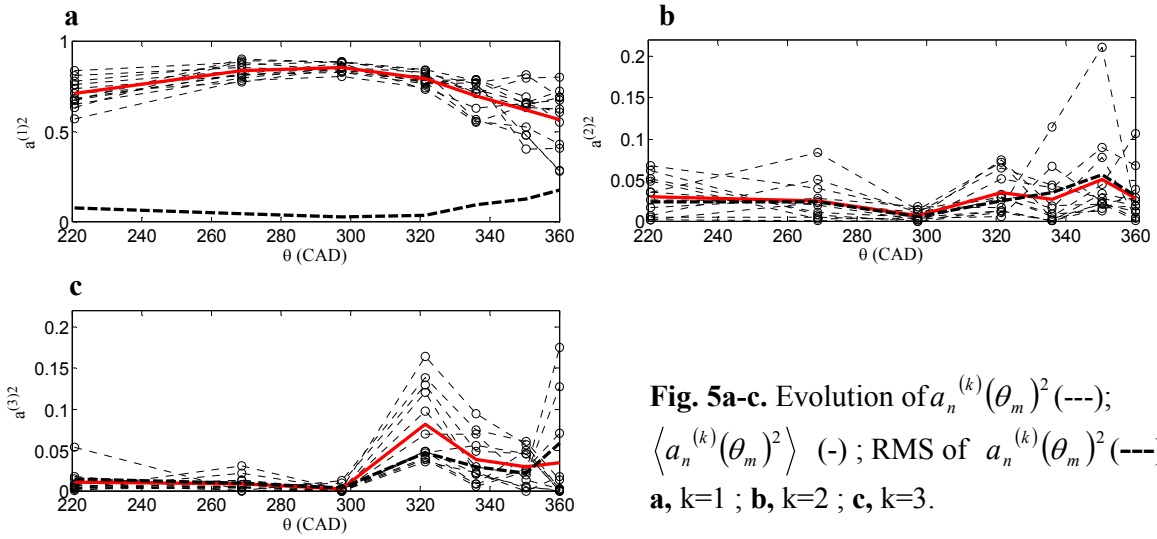

Fig. 5a-c. Evolution of $a_n^{(k)}(\theta_m)^2$ (---); $\left\langle a_n^{(k)}(\theta_m)^2 \right\rangle$ (-) ; RMS of $a_n^{(k)}(\theta_m)^2$ (**---**) : **a,** k=1 ; **b,** k=2 ; **c,** k=3.

5. Application to the parameters space overview

Because each field is normalised, the POD coefficients obtained here allow detecting a particular structure of the flow field. For instance, if the coefficient associated with mode 2 is large, the swirling motion will be highly displaced in the direction characterised by the second mode. Thus, according to the projection examined, we are able to quantify, among others, the structure of the rotation (first mode) and the displacement of the swirling motion in two privileged directions (second and third mode). The state of the system can therefore be described in term of the first three coupled projections.

For a given CAD, the statistical measurements *(i)* represent a large amount of possible states. Thus, the statistical dataset corresponding to the whole compression stroke is holding a lot of possible states between $\theta = 220$ CAD and $\theta = 360$ CAD. By projecting TRPIV flow-fields on this basis, we catch the likelihood between the time-resolved velocity and the possible states extracted from the statistical fields. In the following, the evolution of the normalized projections $\gamma_n^{(k)}(\theta_m) = \left[a_n^{(k)}(\theta_m) - \left\langle \alpha_n^{(k)}(\theta_m) \right\rangle_\theta \right] / \sigma^{(k)}(\theta_m)$, where $\sigma^{(k)}(\theta_m)$ is the RMS value of $\alpha_n^{(k)}(\theta_m)$, will be examined for the three first POD modes, since the large-scale variation associated with these modes have been identified and these modes dominates the flow. The state of the flow during the compression stroke will be represented by the vector $\left(\gamma_n^{(1)}(\theta_m), \gamma_n^{(2)}(\theta_m), \gamma_n^{(3)}(\theta_m)\right)$.

The question that we had in mind when plotting figure 6 is the following : During one cycle, is the vector $\left(\gamma_n^{(1)}(\theta_m), \gamma_n^{(2)}(\theta_m), \gamma_n^{(3)}(\theta_m)\right)$ staying in one particular sub-region of the parameter space (a region which would then change from cycle to cycle) or do the vector $\left(\gamma_n^{(1)}(\theta_m), \gamma_n^{(2)}(\theta_m), \gamma_n^{(3)}(\theta_m)\right)$ evolves over the whole parameter space ? Of course, 12 consecutive cycles is a too small sample to conclude in a statistical sense. However, a clear indication from figure 6 is that for most time-resolved cycles, the trajectory of $\gamma_n^{(k)}$ exhibit several "zero crossing points" during a single compression (although some trajectories showing quasi-constant $\gamma_n^{(k)}$ are detected). This means that the structure of the flow can vary significantly during one cycle and that we see no clear dependence of the in-cycle evolution to the parameters measured in this PIV plane at $\theta = 220°$. Figure 6a-c highlights the trajectory of $\gamma_8^{(1)}(\theta_m), \gamma_8^{(2)}(\theta_m)$ and $\gamma_8^{(3)}(\theta_m)$.

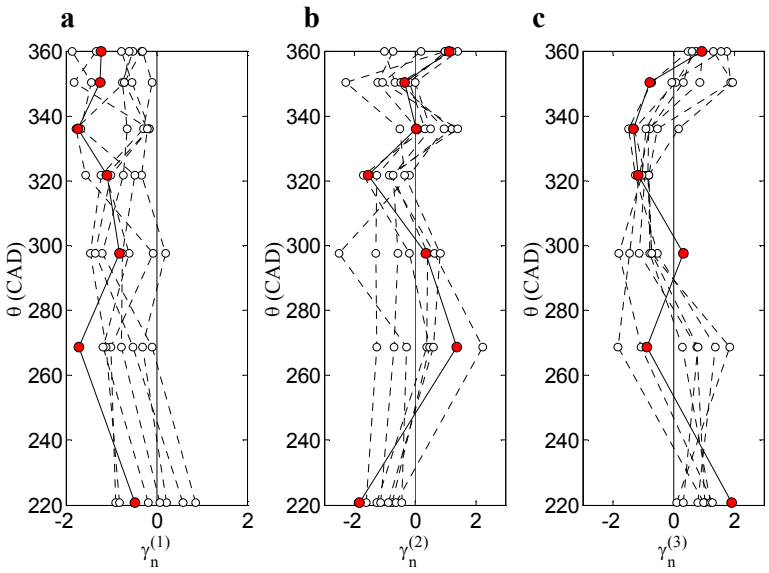

Fig. 6a-c. Trajectories of the normalized projections $\gamma_n^{(1)}(\theta_m), \gamma_n^{(2)}(\theta_m), \gamma_n^{(3)}(\theta_m)$. Red dot correspond to the eighth cycle : **a,** $\gamma_8^{(1)}(\theta_m)$; **b,** $\gamma_8^{(2)}(\theta_m)$; **c,** $\gamma_8^{(3)}(\theta_m)$.

In this particular cycle, interesting features can be detected - for instance, $\gamma_8^{(1)}(\theta_m) < 0$ along the compression stroke. The deviation of the fluid motion from a mean swirling structure, represented by the first POD mode, is then low. Figures 6b and 6c reveal a strong variation of the second and third parameters trajectory. The displacement of the swirling flow is high at the beginning of the compression stroke, since $\gamma_8^{(3)}(\theta_m = 220°) \approx -\gamma_8^{(2)}(\theta_m = 220°) \approx -2$. At $\theta \approx 300°$, the value of both parameters is much lower. Consequently, the swirling motion has been centred within the chamber until the middle of the compression stroke, since the displacement of the flow was strongly reduced. Moreover, we notice that a positive value of $\gamma_8^{(2)}(\theta_m)$ corresponds, three crank angles out of seven, to a negative value of $\gamma_8^{(3)}(\theta_m)$. This could therefore be used to identify a correlation between the displacement in the directions hold by the second and third modes. This point is currently under study.

6. Concluding remarks

A coupling approach between TRPIV data obtained in a transparent motored Diesel engine and a phase-invariant POD procedure was discussed in this paper. The research engine was developed by RENAULT s.a.s. in order to improve the understanding of the cyclic variations of the swirling flow. These time-resolved data were obtained in severe thermodynamical conditions both in the cylinder and the bowl during many consecutive cycles. First, we focused the discussion on the two datasets used for the analysis: the statistical dataset and the time-resolved one. The experimental configuration for both measurements has been described. An extension of the classical POD has been applied on the statistical fields. This application, called phase-invariant POD takes into account all the phases corresponding to the compression stroke. Such a process allows having a well defined POD basis, in a convergence sense. We show that the flow could be well-described by the three first eigenmodes. The first one can be used to quantify the structure of the swirling motion. The two other modes contribute to the displacement of the flow inside the chamber.
As the measurements used to build the basis are not temporally resolved, TRPIV flow-fields are then introduced through a coupling methodology. The time-resolved measurements were projected back to the converged POD basis. This approach gave a clear description of the compressed flow dynamics. We prove that the fluctuations associated with both the intensity and the displacement of the swirling motion increases during the compression stroke, particularly during the transfer in the bowl.. Finally, dynamics is introduced through the study of the normalized projections associated with the fluctuations identified. We have shown that the coefficients can vary over the full parameter space during one compression.
We insist on the fact that the coupling approach developed here can be applied to DNS or LES data provided a reliable POD basis is found. The state has been here regarded as a combination of structure of swirl and displacement. Influence of higher POD modes on the flow features should also be investigated. The method we proposed in this paper could obviously be used in such an aim.

Acknowledgements

We wish to thank Dr. C. Tanguy for its helpful technical support regarding measurements. We thank Dr. G. Charnay and Dr. J. Moreau for their participation in this research work. The technical support of C. Dauphin is also greatly acknowledged.

References

Arcoumanis C; Hadjiapostolou A; Whitelaw JH (1987) Swirl centre precession in engine flow. SAE 870370

Baby X; **Floch A** (1997) Investigation of the In-cylinder tumble motion in a multi-valve engine : effect of the piston shape. SAE 971643

Berkooz G; Holmes P; Lumley JL (1993) The proper orthogonal decomposition in the analysis of turbulent flows. Annual review fluid mechanics **25**:539-75

Bonnet JP; Delville J; Glauser MN (2002). Coherent structures in turbulent shear flows: the confluence of experimental and numerical approaches. Proceedings of ASME Fluids Engineering division summer meeting,. Montreal, Quebec, Canada, July 14-18. FEDSM2002-31412

Borée J; Maurel S; **Bazile R** (2003) Disruption of a compressed vortex. Phys. of fluids 14-7

Cosadia I; Borée J; Charnay G; Dumont P (2006) Cyclic variations of the swirling flow in a Diesel transparent engine. Accepted in Experiments in Fluids.

Deslandes W ; Dumont P ; Dupont A ; Baby X ; Charnay G ;Boree J (2004) Airflow cyclic variation analysis in diesel combustion chamber by PIV measurements. SAE 2004-01-1410

Druault P ; Guibert P ; Alizon F (2005) Use of proper orthogonal decomposition for time interpolation from PIV data. Experiments in Fluids

Enotiadis AC ; Vafidis C ; Whitelaw JH (1990) Interpretation of cyclic flow variations in motored internal combustion engines. Experiments in fluids **10**:77-86

Fogleman M; Lumley JL; Rempfer D; Haworth D (2004) Application of the proper orthogonal decomposition to datasets of internal combustion engine flows. Journal of turbulence 5.

Graftieaux L; Michard M; Grosjean N (2001) Combining PIV, POD and vortex identification algorithms for the study of unsteady turbulent swirling flows. Measurement Science and technology 12:1422-1429.

Holmes P; Lumley J; Berkooz G (1996) Turbulence, Coherent Structures, Dynamical Systems and Symmetry. Cambridge Monographs on Mechanics.

Heywood JB (1988) Internal combustion engine fundamentals. McGraw-Hill.

Hill PG ; Zhang D (1994). The effects of swirl and tumble on combustion in spark-ignition engines. Prog. Energy Combust. Sci. **20**: 373-429.

Lecordier B (1997). Etude de l'interaction de la propagation d'une flamme prémélangée avec le champ aérodynamique par association de la tomographie laser et de la vélocimétrie par image de particules. PhD thesis of Faculté des Sciences de l'Université de Rouen.

Lumley JL (1967). The structure of inhomogeneous turbulence. Proceedings Atmospheric turbulence and radio-wave propagation Yaglom and Tatarski, eds Nauka, Moskow pp166-178.

Lumley JL (1999) Engines, an introduction. Cambridge university press.

Patte-Rouland B; Lalizel G ; Moreau J ; Rouland E (2001) Flow Analysis of an Annular Jet by Particle Image Velocimetry and Proper Orthogonal Decomposition. Measurement Science and Technology. **12**. pp. 1404-1412.

Payri F; Desantes JM; Pastor JV (1996) LDV Measurements of the flow inside the combustion chamber of a 4-valve D.I. diesel engine with axisymetric piston bowls. Experiments in fluids **22**:118-128.

Reuss DL; Adrian RJ; Landreth CC; French DT; Fansler TD (1989). Instantaneous planar measurements of velocity and large-scale vorticity and strain rate in an engine using particle image velocimetry. SAE technical papers 890616.

Sirovich L (1987). Turbulence and the dynamics of coherent structures, part I: coherent structures. Quarterly of applied mathematics **45-3**:561-571.

Towers DP; Towers CE (2004) Cyclic variability measurements of in-cylinder engine flows using high-speed particle image velocimetry. Measurement Science and Technology. **15:**1917-1925.

Westerweel J (1993). Digital particle image velocimetry, theory and application. Delft university press.